Volume 11
Number 21
7 November 2024
Pages 5125–5452

Materials Horizons

rsc.li/materials-horizons

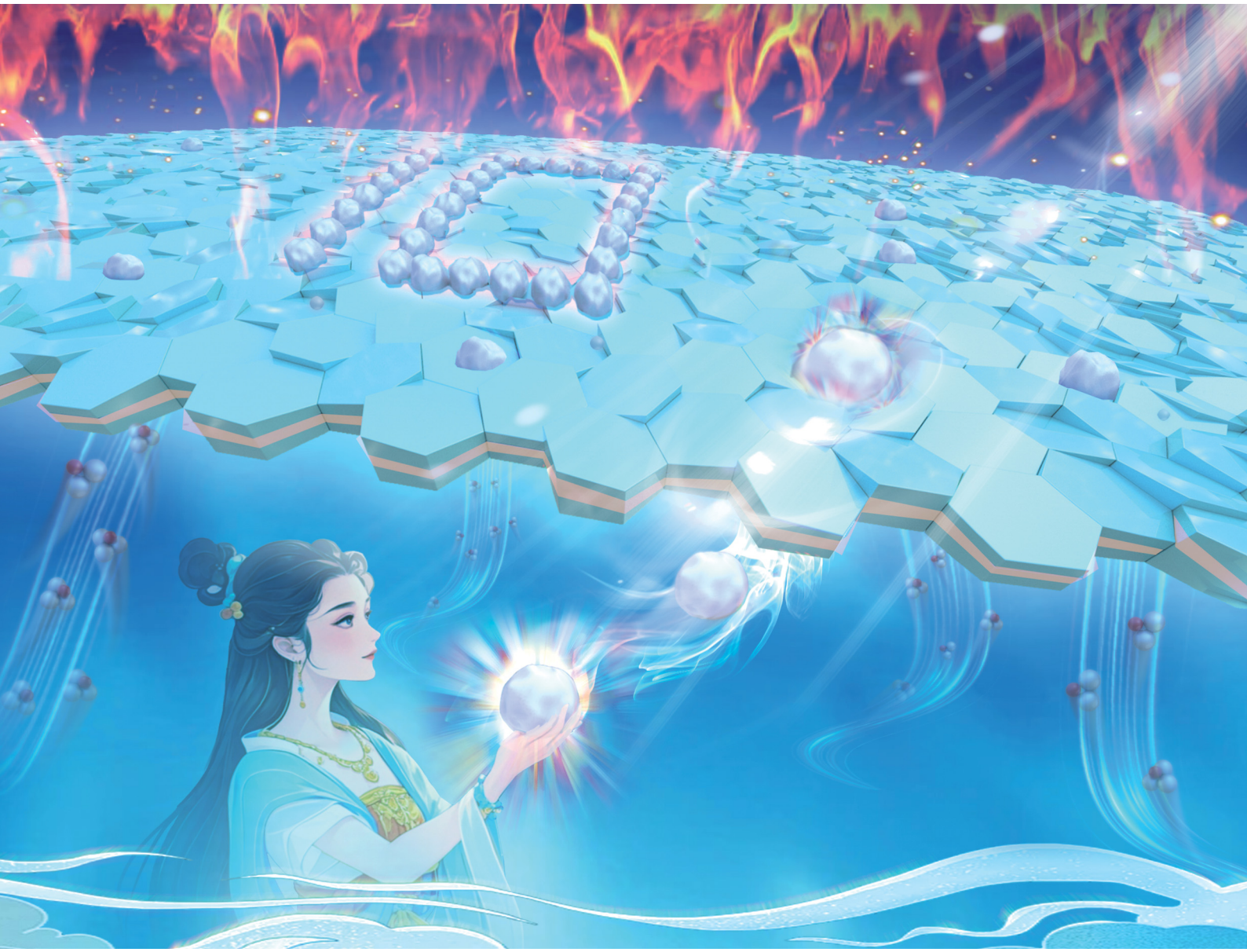

ISSN 2051-6347

ROYAL SOCIETY OF CHEMISTRY

COMMUNICATION

Siming Ren, Liping Wang *et al.*
Enhanced environmental adaptability of sandwich-like MoS_2/Ag/WC nanomultilayer films *via* Ag nanoparticle diffusion-dominated defect repair

10 YEARS ANNIVERSARY

Materials Horizons

ROYAL SOCIETY OF CHEMISTRY

COMMUNICATION

View Article Online
View Journal | View Issue

Cite this: *Mater. Horiz.*, 2024, 11, 5230

Received 6th July 2024,
Accepted 12th September 2024

DOI: 10.1039/d4mh00867g

rsc.li/materials-horizons

Enhanced environmental adaptability of sandwich-like MoS_2/Ag/WC nanomultilayer films *via* Ag nanoparticle diffusion-dominated defect repair†

Min Yang,[ab] Xin Fan,[ab] Siming Ren *[a] and Liping Wang *[a]

Robustness and environmental adaptability are crucial for molybdenum disulfide (MoS_2) films to minimize friction and wear in industrial applications. However, current sputtered MoS_2 films suffer from inherent defects, including insufficient hardness, poor crystallinity, and susceptibility to oxidation, thereby limiting their longevity and reliability. Here, we present a sandwich-like nanomultilayer architecture comprising alternating MoS_2 and tungsten carbide (WC) layers integrated with Ag nanoparticles. This architecture demonstrates robust corrosion resistance, effectively protecting the MoS_2 within the film for over 18 months of air exposure and exhibiting minimal corrosion during 21 days of salt spray tests. The remarkable environmental stability of the sandwich-like MoS_2/Ag/WC nanomultilayer film is attributed to the creation of numerous heterogeneous interfaces and the spontaneous diffusion and repair of Ag atoms through defect channels of the film, impeding the penetration of corrosive agents. Furthermore, during the frictional process, Ag, characterized by its inherent high mobility and ductility, facilitates the formation of a dense tribofilm on its counterpart ball, encapsulating formed metal oxides to prevent adhesive wear. As a result, the film exhibits a significantly reduced wear rate (1.25×10^{-7} mm^3 N^{-1} m^{-1}) even after long-term salt spray corrosion and air exposure. This study offers a general route for designing MoS_2-based materials toward long-lifetime and environmental adaptability *via* self-repair mechanisms.

New concepts

Improving the reliability and environmental adaptability of solid lubricants holds significant promises for diverse engineering applications and has been a longstanding pursuit in history. Although existing studies have shown the efficacy of incorporating functional elements to mitigate friction and extend the lifespan of MoS_2 films in air, there have been no reports on the environmental responsiveness and self-repair capabilities of MoS_2-based lubricating films. We present a pioneering approach to realize a smart sandwich-like nanomultilayer architecture with exceptional corrosion resistance and atmospheric tribological performance. This achievement stems from the meticulous design of lubricating MoS_2 layers, load-bearing WC layers, and the incorporation of Ag nanoparticles. Spontaneous diffusion of Ag atoms into the film surface occurs through inherent defects within the film, effectively repairing the defects and imparting ultrahigh environmental stability. Significantly, Ag atoms can also repair the sliding interface, enhance the bonding strength of the tribofilm, and wrap the friction-induced oxide nanoparticles with the MoS_2 nanosheets, thereby achieving low friction and long lifetime even under long-term corrosion conditions. Our finding offers a novel strategy for designing smart solid lubricants that may lead to revolutionary applications under harsh operating conditions.

1. Introduction

Friction and wear are common physical phenomena. Approximately 30% of the world's primary energy consumption is attributed to friction, and wear is responsible for around 80% of mechanical part failures.[1–4] To mitigate these effects, various strategies have been historically proposed and adopted, among which the use of solid lubricants stands out as particularly effective.[5] Molybdenum disulfide (MoS_2)-based films represent a significant class of solid lubricant materials, particularly in environments where liquid lubricants are impractical, such as space technology, mechanical seals, and automotive applications.[6] These films demonstrate ultralow friction and wear under high vacuum and dry inert atmospheres, due to the easy-shear interfaces between atomic layers and strong Mo–S covalent bonding within the basal plane.[7–9] However, the tribological properties of MoS_2-based films deteriorate significantly in the presence of humidity or oxygen, which hinders their practical utility under terrestrial atmospheric conditions.[10,11]

Numerous studies have shown that incorporating metal, nonmetal elements, and other compounds represents a predominant approach to enhance the structural density and

[a] *Key Laboratory of Advanced Marine Materials, Ningbo Institute of Materials Technology and Engineering, Chinese Academy of Sciences, Ningbo 315201, China. E-mail: rensiming@nimte.ac.cn, wangliping@nimte.ac.cn*

[b] *University of Chinese Academy of Sciences, Beijing 100049, China*

† Electronic supplementary information (ESI) available. See DOI: https://doi.org/10.1039/d4mh00867g

mechanical properties of MoS_2 films, thereby reducing friction and wear in humid air.[12–17] Despite improving the humidity resistance of MoS_2, the durability of these composite films under severe conditions remains inadequate. Additionally, doping often leads to an amorphous or random-oriented structure in MoS_2 films, which compromises their moisture resistance compared to the MoS_2 (002) plane parallel to the substrate.[18,19] Conversely, leveraging the ''hard'' and ''tough'' characteristics of nanomultilayer structures enhances the tribological performance relative to single-layer and composite films.[20,21] This design promotes the preferential growth of MoS_2 (002) planes parallel to the substrate, inhibiting the penetration of corrosive species and broadening the application range of MoS_2 films.[22,23] Prior experimental findings show that a nano-alternating multilayer structure comprising MoS_2 and WC effectively exerts synergistic effect of the two materials, achieving robust ultra-low friction (0.006) in vacuum.[23] However, such a film generates significant wear debris when subjected to friction tests in air, mainly attributed to the difference in mechanical properties between MoS_2 and ceramics. Furthermore, defects and pores inevitably occur in sputtered MoS_2-based films, serving as preferential reaction sites of aggressive species, which will decrease the efficiency of MoS_2 and shorten the lifespan of the films.[24] Developing a robust MoS_2-based film with self-repair capabilities and prolonged operational life remains a critical challenge, given its importance in diverse engineering applications.

Self-repair of defects or damage typically requires the presence of a mobile phase. Traditional self-repairing films are classified into extrinsic and intrinsic types. Extrinsic self-repairing films involve embedding microcapsules or nanocontainers filled with healing agents or corrosion inhibitors within a polymer matrix. Upon damage, these capsules rupture, releasing the healing agents or inhibitors to repair the damage and prevent further corrosion. Intrinsic self-repairing films rely on reversible interactions between resin molecules or between these molecules and functional additives to repair defects.[25,26] While these methods are effective for organic polymer films, they are not suitable for physical vapor deposition (PVD) films. Recent studies have shown that introducing a functional factor (*i.e.*, a mobile phase) directly during the film deposition process can address defects through physical diffusion.[27,28] This method repairs defects without altering the composition or structure of films, offering a practical solution for PVD films.

Silver nanoparticles (Ag NPs), known for their high mobility and mechanical flexibility,[29–31] have been effectively employed to heal defects in Cu substrates,[32] conductive inks,[33] and cracks in coatings.[34] When dispersed at the interfaces between MoS_2 and ceramic multilayers to form a sandwich-like structure, Ag NPs serve as functional agents. They not only enhance the bonding strength of the MoS_2/ceramic interface but also exhibit a propensity for adhering to the ball surfaces, forming stable transfer films that contribute to reduced friction and wear. Importantly, the ductile nature of Ag enables it to act akin to a high viscosity fluid,[35,36] facilitating the repair of sliding interfaces during frictional processes.

Encouraged by these good promises, we created a sandwich-like MoS_2/Ag/WC nanomultilayer film capable of providing exceptional corrosion resistance and atmospheric tribological performance, attributed to its self-repair capabilities. Using detailed spatial component analysis, we have shown that the spontaneous diffusion of Ag NPs plays a unique role in achieving these outstanding properties. Ag NPs can spontaneously diffuse toward the film surface through inherent defects, thereby repairing these defect channels and preserving the lubricating performance of MoS_2. Furthermore, compared to typical multilayer structures, our study highlights that the sandwich-like MoS_2/Ag/WC architecture exhibits enhanced capability to repair the transfer film, promoting the formation of smooth sliding interfaces that mitigate abrasive wear and achieve ultralow wear rates.

2. Results and discussion

2.1 Composition, morphology and structure of the sandwich-like nanomultilayer film

As shown in Fig. 1, the designed MoS_2/Ag/WC nanomultilayer film was fabricated alongside reference samples (Pure MoS_2, MoS_2/Ag and MoS_2/WC films) using a non-equilibrium magnetron sputtering system (see the Experimental details section). X-ray photoelectron spectroscopy (XPS) was employed to analyze the surface chemical bonding of the as-prepared films (see Fig. S1 and S2 in the ESI†). Prior to analysis, a high-energy Ar ion beam accelerated at 2 keV for 3 min was used to remove the oxidized surfaces of the films during air exposure. Analysis of the Mo 3d and W 4f spectra demonstrates that the MoS_2/Ag/WC film is composed of MoS_2, MoS_{2-x}, WC_{1-x}, Ag, and a minor fraction of free carbon. The presence of MoS_{2-x}, WC_{1-x}, and free carbon suggests sulfur and carbon deficiencies, likely resulting from preferential resputtering of these light elements during plasma-assisted film growth.[23,37,38] The MoS_2/Ag/WC nanomultilayer film exhibits a characteristic cauliflower-like surface morphology, with a surface roughness (13.4 nm), higher than that of pure MoS_2 (6.4 nm), MoS_2/Ag (9.5 nm), and MoS_2/WC (5.0 nm) films, attributed to increased grain size (Fig. S3, ESI†). Nevertheless, compared to these films, the MoS_2/Ag/WC nanomultilayer film shows a reduced grain gap and more compact structure. The multilayered interfaces effectively inhibit the growth of MoS_2 columnar crystals, resulting in a denser structure, as observed in the cross-sectional morphology (Fig. S3D, ESI†). Additionally, the presence of Ag promotes grain growth and helps fill grain boundaries due to its high mobility.

To characterize the microstructure of the MoS_2/Ag/WC film, a cross-sectional lamellar specimen was prepared using a focused ion beam (FIB) slicing technique and examined by transmission electron microscopy (TEM) (Fig. 2(A)). The film comprises a Ti adhesion layer, a Ti/MoS_2/Ag/WC gradient transition layer, and an alternating MoS_2/Ag/WC nanomultilayer. As expected, the high-angle annular dark-field (HAADF) image and corresponding electron dispersive spectroscopy (EDS) mapping confirm a gradual increase in Mo, S, and W content within the gradient transition layer, accompanied by a decrease in the Ti content from the substrate towards the surface (Fig. 2(B)). Agglomeration of Ag NPs in this region is

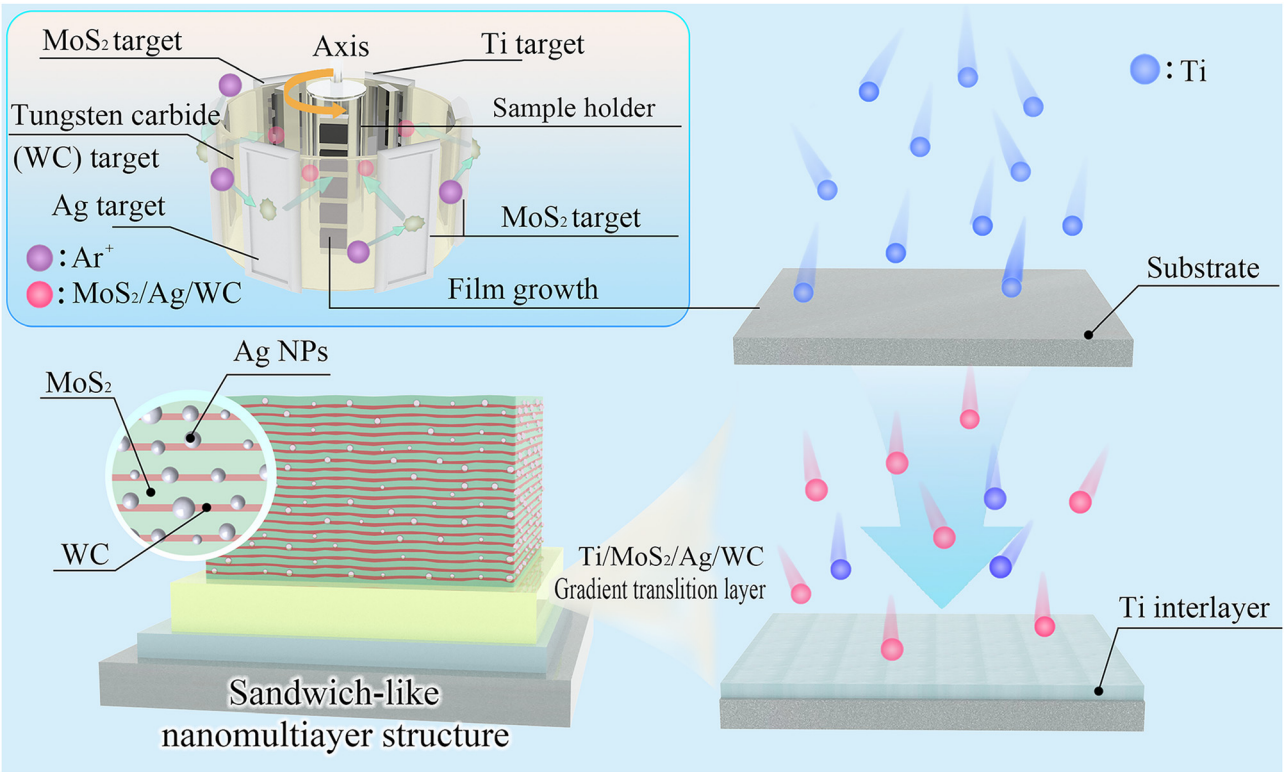

Fig. 1 Schematic illustrating the fabrication and structural design of the sandwich-like MoS_2/Ag/WC nanomultilayer film.

attributed to upward diffusion of Ag during deposition, with a higher Ag content in the gradient transition layer compared to the nanomultilayer, influenced by rapid sample holder rotation at this deposition stage. Local TEM micrograph (Fig. 2(C)) reveals a well-defined nanomultilayer structure, with randomly distributed black nanoparticles at the MoS_2/WC interface forming a sandwich-like arrangement. Detailed high-resolution TEM (HRTEM) imaging shows individual MoS_2 and WC layer thicknesses of approximately 23.3 nm and 6.5 nm, respectively. Fast Fourier transform (FFT) analysis (Fig. 2(D), inset) of selected nanocrystalline grain shows a lattice spacing of 0.24 nm, corresponding to the (111) interplanar distance of Ag. MoS_2 predominantly grows along the (002) crystal planes parallel to the substrate, whereas WC exists in an amorphous state. This results in a novel sandwich-like structure composed of highly oriented MoS_2 and amorphous WC nanolayers intermixed with Ag NPs, contrasting sharply with the MoS_2/Ag composite film and MoS_2/WC nanomultilayer film (Fig. S4, ESI†). In the X-ray diffraction (XRD) analysis (Fig. 2(E)), the MoS_2/Ag/WC nanomultilayer film exhibits a prominent diffraction peak at $\sim 12^\circ$, corresponding to the (002) plane of MoS_2, which is consistent with TEM observations. Films with highly ordered MoS_2 (002) planes are known for reduced friction and enhanced environmental stability compared to other crystallographic orientations.

2.2 Mechanical properties of the nanomultilayer films

To assess the mechanical behavior of MoS_2/WC and MoS_2/Ag/WC nanomultilayer films, indentation experiments were conducted, and the indentation morphologies were characterized using a scanning electron microscope (SEM) (Fig. 3(A) and (B)). Up to a normal load of 50 mN, no cracks are observed in either the MoS_2/WC or MoS_2/Ag/WC nanomultilayer films, demonstrating that the nanomultilayer structure effectively enhances the mechanical properties of MoS_2. Notably, numerous white particles appear in the indentation area of the MoS_2/Ag/WC film, confirmed by EDS as Ag-rich particles (Fig. S5, ESI†), indicating precipitation of Ag atoms along grain boundaries and significant recrystallization under cold deformation of the film.[39] To further understand the micro-mechanical differences between MoS_2/WC and MoS_2/Ag/WC nanomultilayer films, scanning probe microscopy (SPM) was employed to perform nanoscopic wear tests under gradient loading. A $2 \times 2\ \mu m^2$ area was selected, and the normal load was gradually increased from 500 nN to 15 μN. The diamond probe was scanned repeatedly to observe the wear behaviors and changes in film morphology.[40] As depicted in morphology images (Fig. 3(C) and (D)), with increasing load, MoS_2/WC film exhibits evident plastic deformation and accumulation of wear debris around the tested area edges, whereas minimal morphology change occurs in the MoS_2/Ag/WC film. Generally, the node where two profiles of the same wear trajectory first diverge and no longer coincide is defined as the transition from elastic to plastic deformation.[40–42] As shown in Fig. 3(E) and (F), corresponding 2D profiles illustrate that the MoS_2/Ag/WC film presents greater elastic deformation capability ($\sim$4.5 μN) than that of the MoS_2/WC film ($\sim$2.5 μN). Consequently, the sandwich-like film exhibits superior resistance to microplastic deformation, indicative of higher yield strength,

thereby achieving robust wear resistance.[43] This exceptional resistance to mechanical damage and nanoscale wear holds promise for broader applications in engineering.

2.3 Environmental stability of the films

The corrosion resistance of the sandwich-like MoS_2/Ag/WC nanomultilayer film and reference samples was evaluated using the standard ASTM B117 salt spray test over a total duration of 21 days (Fig. 4(A)). The surface morphologies of the films were observed using an optical microscopy every 7 days during the salt spray exposure (Fig. S6, ESI†). Before salt spray tests, all samples show smooth surfaces and uniform color without noticeable oxidation. After 7 days of salt spray, significant corrosion is observed in localized areas of pure MoS_2 and MoS_2/Ag films, while the surface morphology of MoS_2/WC nanomultilayer film shows minor change compared to its as-prepared state, and the sandwich-like MoS_2/Ag/WC nanomultilayer film exhibits randomly distributed dark spots on the surface. By day 14, corrosion has expanded further in the pure MoS_2 and MoS_2/Ag films, with some regions experiencing film rupture and exfoliation due to corrosion products, indicating film failure. The inferior corrosion resistance of pure MoS_2 and MoS_2/Ag films can be attributed to their porous and columnar structure (Fig. S3, ESI†). In contrast, the overall surface color of the MoS_2/WC film becomes darker, and the appearance of the MoS_2/Ag/WC film resembles its condition after 7-day exposure. By day 21 (Fig. 4(B) and (C)), the surface color (labelled as Area I) of the MoS_2/WC film is further darkened. In the MoS_2/Ag/WC nanomultilayer film, most of the surface (labelled as Area II) remains smooth, with some local areas (Area III) showing large dark patches.

To further investigate the corrosion behavior of MoS_2/WC and MoS_2/Ag/WC nanomultilayer films following the 21-day corrosion tests, SEM was employed (Fig. 4(D) and (E)). The results manifest numerous micro-scale corrosion pits on the surface of the MoS_2/WC film, indicating preferential oxidation of MoS_2 through film defects. The resulting corrosion products lead to local volume expansion and exfoliation. Subsequent exposure of fresh edges causes horizontal expansion of the corrosion area, displaying layer-by-layer peeling morphology. This observation is corroborated by the SPM image (Fig. 4(F)). In contrast, the MoS_2/Ag/WC nanomultilayer film exhibits a uniform and smooth surface morphology in Area II (Fig. 4(E)), with significantly reduced surface roughness (~5.7 nm, Fig. 4(G)) compared to the as-prepared sample (~13.4 nm). This reduction is presumably due to the accelerated diffusion

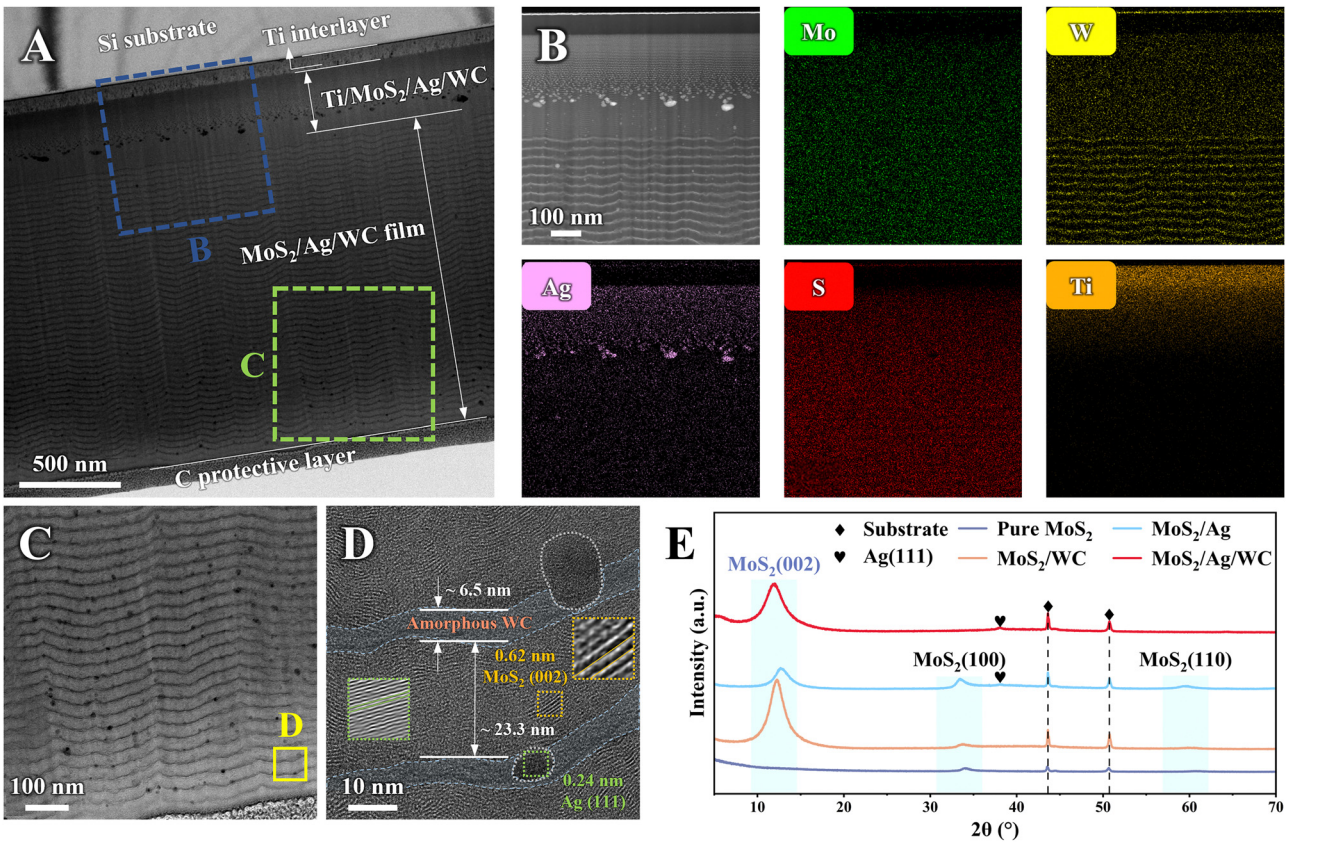

Fig. 2 Structural characterization and interface analysis of sandwich-like MoS_2/Ag/WC nanomultilayer film. (A) Cross-sectional TEM image showing the layered structure of the MoS_2/Ag/WC film. (B) STEM-HAADF image of the region marked by the blue rectangle, accompanied by elemental maps highlighting Mo, W, Ag, S, and Ti distributions. (C) Enlarged view of the region marked by the green rectangle in (A), illustrating the distinct multilayer structure. (D) HRTEM image of the region marked in (C), showing the Ag nanoparticles embedded between the MoS_2 and WC layers, forming a sandwich-like structure. (E) XRD patterns comparing MoS_2, MoS_2/Ag, MoS_2/WC, and MoS_2/Ag/WC films.

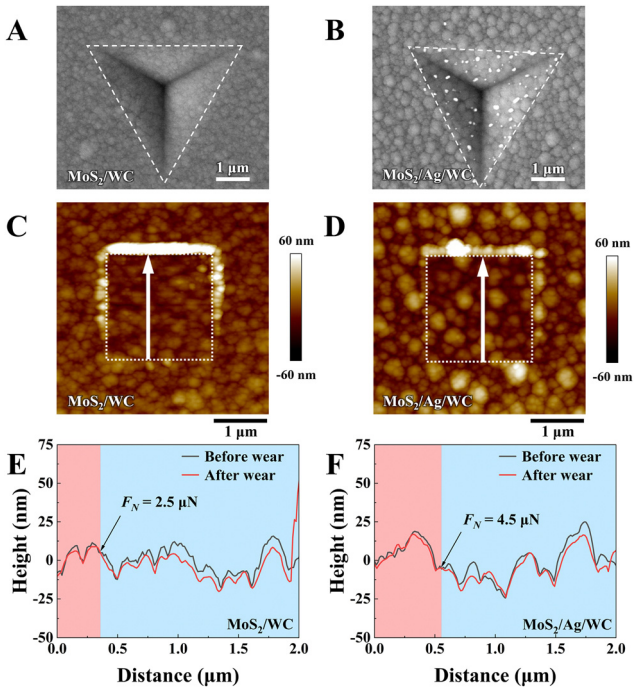

Fig. 3 Micro-mechanical properties of MoS_2/WC and MoS_2/Ag/WC nanomultilayer films. (A) and (B) SEM images of indentations from 50 mN nanoindentation tests performed on MoS_2/WC and MoS_2/Ag/WC nanomultilayer films. (C) and (D) SPM images showing topographical variations of worn surfaces after nano wear tests of MoS_2/WC and MoS_2/Ag/WC nanomultilayer films. Testing areas (2×2 μm^2) and directions marked by white dashed squares and arrows, respectively. (E) and (F) Corresponding 2D profiles along the white arrows marked in (C) and (D), respectively.

of Ag atoms in the salt spray environment, which fills gaps between grains and results in a smoother surface. Interestingly, surface potential measurements using a Kelvin probe force microscope (KPFM) equipped in SPM indicate a decrease from −0.032 V in Area II to −0.170 V in Area III (Fig. 4(H) and (I)). Changes in conductivity and polarization typically account for variations in surface potential.[44] Notably, the significant decrease in surface potential in Area III suggests a low electron doping effect,[45] indicating that the appearance of change in this area is not caused by oxidation of the film composition.

Building upon the aforementioned findings, we conducted further characterization of Area III identified on the MoS_2/Ag/WC film by TEM (Fig. 4(J)). Remarkably, EDS and HRTEM results confirm an enrichment of Ag NPs belonging to the (111) crystal plane is observed on the film surface (Fig. 4(K) and (L)). Meanwhile, the number of film modulation periods in Area III is consistent with its as-prepared state, indicating that no significant corrosion occurs in this region (Fig. S7, ESI†). This indicates that Ag NPs within the film diffused to the surface driven by salt spray, where they were enriched in the local areas to form a protective layer, thus inhibiting the diffusion of the aggressive species.[46]

In addition to Ag NPs, strong signals of amorphous carbon (a-C; 1335 and 1576 cm^{-1} corresponding to the D and G peaks) were detected in Area III (Fig. 4(M)).[47] Previous studies have demonstrated a spontaneous charge transfer phenomenon between Ag atoms and free carbon atoms, as well as carbon atoms in WC, indicating a strong interaction between Ag and C atoms.[39,48] As Ag atoms diffuse through defects in the film, they adsorb near C atoms and migrate to the film surface, enriching in the process. Therefore, the detection of the a-C signal in the area enriched with Ag NPs reflects this interaction. To verify this, vacuum heat treatment was performed on the MoS_2/Ag/WC film. It is observed that elevated temperatures significantly accelerate the diffusion of Ag atoms, leading to their aggregation on the film's surface and subsequent Ag NPs formation (Fig. S8, ESI†). Notably, the C content associated with the Ag NPs is found to be distinctly higher compared to other regions.

2.4 Diffusion kinetic behavior of Ag

After a 21-day salt spray test, significant structural changes are found in the MoS_2/Ag/WC film compared to its as-prepared state. Specifically, surface-proximal areas exhibit notable deformation, particularly the region marked by a yellow rectangle in Fig. 5(A) (left panel). It is noteworthy that Ag NPs are obviously enriched within the WC nanolayers or at the MoS_2/WC interface, demonstrating that the diffusion, aggregation, and growth of Ag NPs primarily occur in the amorphous WC nanolayers. As the Ag NPs continue to grow, the WC nanolayers gradually undergo distortion and deformation, resulting in the evolution from nanomultilayers to composite structures. To further uncover the underlying diffusion kinetics of Ag within the film, we exposed the MoS_2/Ag/WC film, which had undergone a 21-day salt spray test, to atmospheric conditions for another 18 months. Subsequently, the cross-sectional morphology and composition of Area III were characterized using TEM-EDS and atomic probe tomography (APT). Upon prolonged atmospheric exposure, Ag NPs continue to diffuse spontaneously along defects or WC nanolayers in the film, making it difficult to distinguish the MoS_2/WC interfaces in many areas (marked right in Fig. 5(A)). Microscopic morphology analysis combined with EDS mapping also shows that some Ag NPs have completely diffused and evolved into Ag-deficient regions (Fig. 5(B)).

The composition depth profiles of the MoS_2/Ag/WC film obtained by APT are shown in Fig. 5(C). The profiles reveal high content of Ag and C in the top surface region, underscoring the strong interaction between Ag and C. Due to upward diffusion, the Ag content significantly decreases in the subsurface region. Importantly, the oxygen content throughout the film, from surface to interior, remains below 2.5 at%, indicating minimal oxidation. This characteristic is crucial for the environmental adaptability and extended service life of the sandwich-like MoS_2/Ag/WC nanomultilayer film. Subsequently, we reconstructed the 3D iso-surface to investigate the diffusion path of Ag atoms. Iso-surfaces generated from higher concentrations of certain atoms typically indicate the presence of large nanoparticles. As shown in Fig. 5(D), the 40 at% Ag iso-surface partially depicts the locations of larger Ag NPs. When the Ag concentration is reduced to 10 at%, we observed an average Ag concentration of 10 at% within the inner region of the film, consistent with the corresponding line concentration

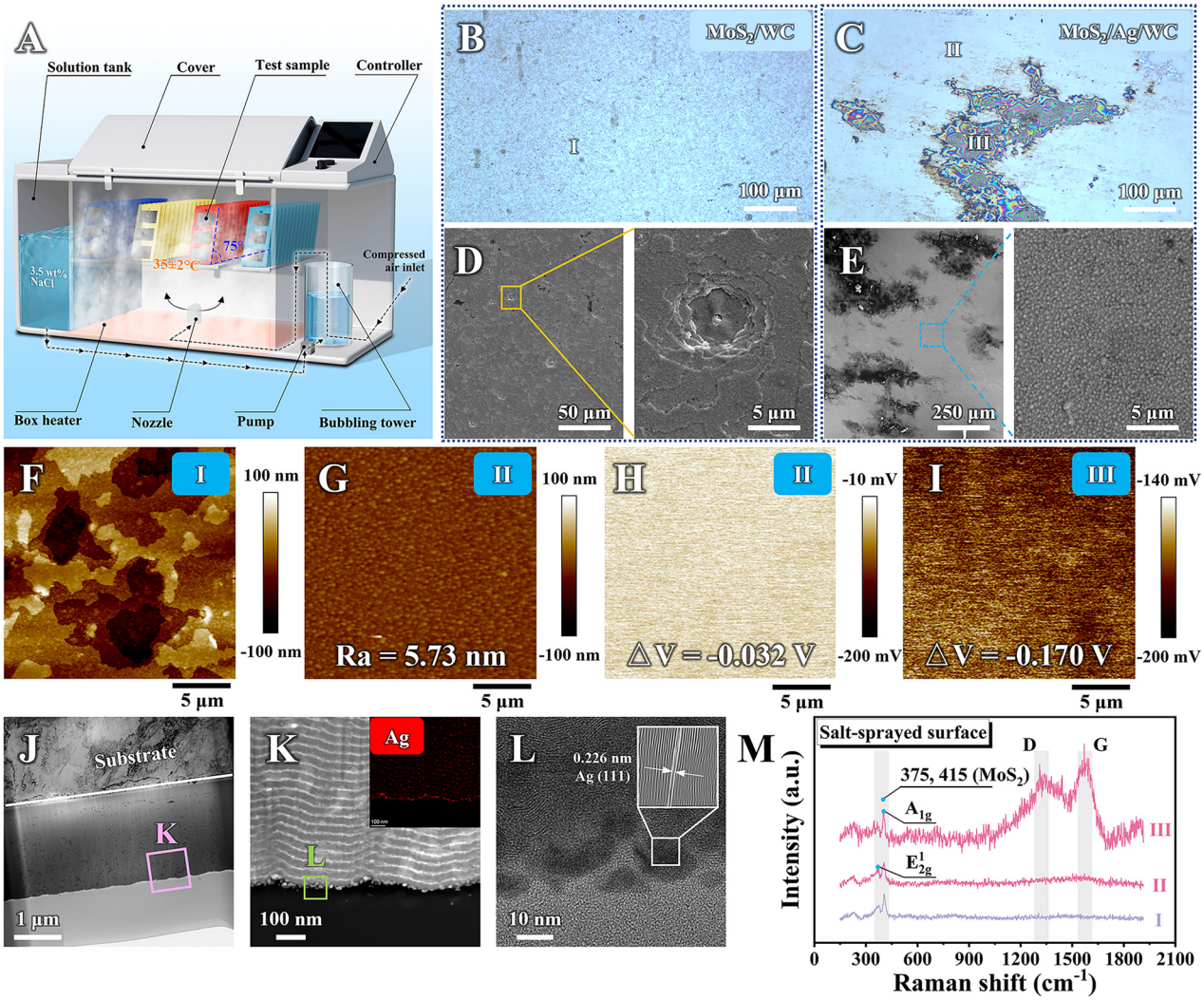

Fig. 4 Salt spray tolerance of the sandwich-like MoS_2/Ag/WC nanomultilayer film and reference samples. (A) Schematic of typical salt spray test and adopted advanced corrosion cycling test chamber used. (B) and (C) Optical images, (D) and (E) SEM images and corresponding enlarged views demonstrating the surface morphologies of MoS_2/WC and MoS_2/Ag/WC nanomultilayer films after 21 days of salt spray test. (F) and (G) SPM images showing the surface topographical variations of region I and II as marked in (B) and (C), respectively. (H) and (I) SPM images showing the surface potential variations of region II and region III as marked in (C), with the corresponding calculated results. (J) Low magnification TEM image depicting the overall cross-section of region III marked in (C). (K) High magnification STEM-HAADF image and corresponding EDS mapping of Ag in the pink square marked in (J). (L) HRTEM image in the green square marked in (K), with the inset showing the identified inverse FFT result. (M) Raman spectra of selected positions labelled in (B) and (C).

distribution results (Fig. 5(C)). In contrast, the iso-surface at lower Ag concentration (1.0 at%) indirectly illustrates the diffusion path of Ag atoms, indicating that Ag atoms first diffuse laterally to specific areas and then along the channels to the surface.

As previously discussed, the exceptional corrosion resistance of the sandwich-like MoS_2/Ag/WC nanomultilayer film depends on the spontaneous diffusion of Ag atoms within the film to repair surface defects, thereby forming a protective Ag nanolayer that blocks the penetration of aggressive species. To further investigate the diffusion behavior of Ag NPs over time, we examined the morphological changes in the as-prepared sandwich-like MoS_2/Ag/WC nanomultilayer films and those exposed to air for 24 months, following different salt spray durations (2 days, 4 days, and 6 days). The surface color of the as-prepared films deepens with extended salt spray time (Fig. S9, ESI†). Conversely, after 24 months of atmospheric exposure, a protective Ag nanolayer forms on the film surface, leading to minimal changes in surface morphology despite different salt spray durations. Nanoindentation was used to create artificial indentations—5 μm in diameter for freshly prepared samples and 1 μm for those exposed to air for 24 months—to assess the evolution of surface morphology, roughness, and potential in relation to salt spray time at a micro-scale (Fig. 6). For the freshly prepared samples, surface roughness initially decreases and then increases with extended

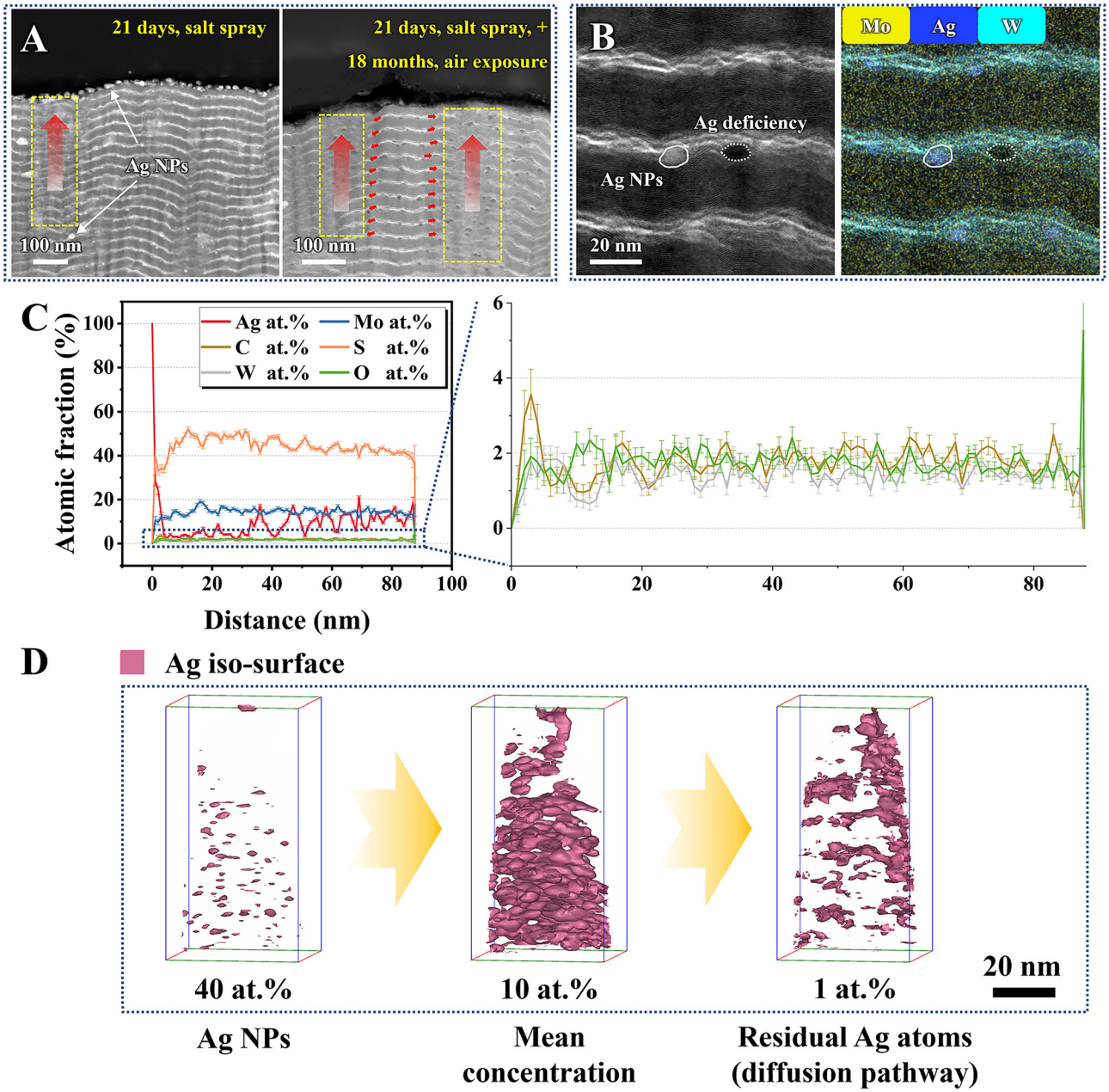

Fig. 5 Detailed characterization of the Ag diffusion path in the sandwich-like MoS_2/Ag/WC nanomultilayer film. (A) Cross-sectional STEM-HAADF images showing the morphologies of the sample after 21 days of salt spraying (left panel) and after salt spraying plus 18 months of air exposure (right panel). The yellow dashed rectangle highlights the fuzzy interfaces of WC layers, and red arrows indicate the direction of Ag migration within the WC layer and toward the top surface. (B) STEM-HAADF image and corresponding EDS map showing Ag NPs and an adjacent Ag deficiency region. (C) Depth concentration profiles and enlarged graph of 0–6 at% obtained by APT. (D) 3D reconstructed iso-surfaces generated by Ag (40 at%, 10 at%, and 1 at%).

salt spray time, while the surface potential consistently decreases (Fig. 6(A) and (C)). Notably, nanoparticles are observed at the indentation areas, indicating that Ag NPs migrate to the film surface. During the initial salt spray stage (2 days), Ag NPs diffuse to grain boundaries and gaps, slightly reducing film roughness (Fig. 6(C)). As salt spray time extends, Ag NPs accumulate on the surface, forming larger particles and significantly increasing roughness, suggesting a dynamic evolution of the film surface. In contrast, for samples subjected to 24 months of atmospheric exposure, both surface roughness and potential show a decreasing trend with increasing salt spray time (Fig. 6(B) and (C)). This trend suggests that extended salt spray exposure accelerates Ag atom diffusion, resulting in a denser and more uniform Ag protective nanolayer on the film surface. Further characterization of three random indentations fabricated on the as-prepared films after 6 days of salt spray (Fig. S10 in the ESI†) reveals significant nanoparticle enrichment. The corresponding EDS maps also confirm the accumulation of Ag and C elements at indentations, indicating that Ag atoms can adsorb amorphous carbon within the film and

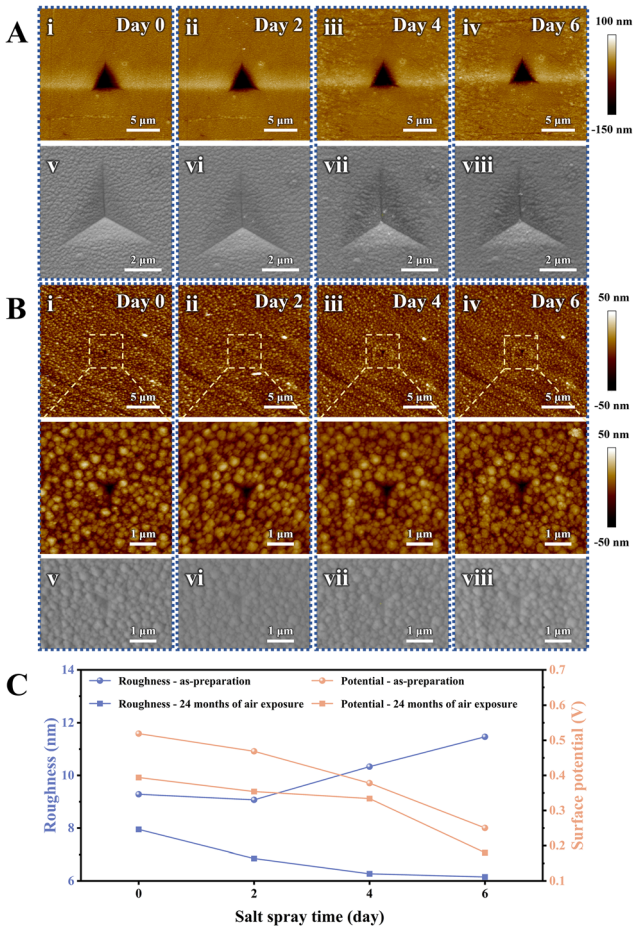

Fig. 6 Time-series *in situ* observation of the sandwich-like MoS_2/Ag/WC nanomultilayer film. (A) and (B) *In situ* SPM (i)–(iv) and SEM (v)–(viii) images showing surface morphology changes of as-prepared sandwich-like MoS_2/Ag/WC nanomultilayer films (A) and those exposed to air for 24 months (B), following salt spray durations of 0, 2, 4, and 6 days. Enlarged views highlight triangle marked by nanoindentation. (C) *In situ* observations of surface roughness and potential variations in the sandwich-like MoS_2/Ag/WC nanomultilayer film. Data are presented for both as-prepared samples and those exposed to air for 24 months.

spontaneously repair the micro-defects such as film grain boundaries, surface scratches, and cracks.

The diffusion pathways of Ag atoms and the self-repair mechanisms of the sandwich-like film are illustrated in Fig. 7. Initially, owing to the high mobility of Ag atoms and their strong interaction with C, Ag atoms at the MoS_2/WC interfaces adsorb surrounding C atoms and diffuse into the amorphous WC nanolayer (as shown in Fig. 5(A)). Guided by energy-favored pathways, Ag atoms enriched with C preferentially diffuse and accumulate at the defective regions of the sputtered film. As Ag NPs grow, the WC nanolayer undergoes deformation and develops cracks, with adjacent WC nanolayers locally connecting to form diffusion channels, thereby transforming the multilayer structure into a multi-component composite (Fig. 5(B) and Fig. S11 in the ESI†). Ultimately, Ag atoms migrate to the film surface through these channels, repairing pores and defects in the surface and subsurface layers, substantially enhancing the environmental adaptability of the film. Cross-sectional TEM images and corresponding EDS Ag maps (Fig. S12 in the ESI†) clearly show an enrichment of Ag NPs on the film surface following both short- and long-term corrosion tests compared to the as-prepared sample.

2.5 Tribological behaviors of the films

To demonstrate the robustness and environmental stability of the sandwich-like MoS_2/Ag/WC architecture, we conducted a comparative study on the friction and wear behaviors of reference MoS_2-based films before and after a 21-day salt spray test (Fig. 8(A)). These films were subjected to a reciprocating sliding test using a GCr15 steel ball (Φ6 mm) under an applied load of 5 N (maximum contact stress of approximately 1 GPa) and at a relative humidity of $\sim$50%. Before the salt spray test, the pure MoS_2 film exhibits failure, while the MoS_2/Ag composite film, MoS_2/WC and MoS_2/Ag/WC nanomultilayer films all completed their sliding mission, confirming that the composite and multilayer structural designs enhance the oxidation resistance of MoS_2. The average friction coefficients of MoS_2/Ag, MoS_2/WC and MoS_2/Ag/WC films are around 0.100, 0.068 and 0.074, respectively (Fig. 8(B)).

Films with a nanomultilayer structure exhibit lower friction coefficients compared to composite films, primarily due to the highly ordered MoS_2 (002) planes aligned parallel to the substrate induced by the nanomultilayer structure (Fig. 2(D) and Fig. S4G in the ESI†). The participation of Ag at the interface increases sliding resistance to some extent, resulting in a slightly higher friction coefficient for the MoS_2/Ag/WC film than for the MoS_2/WC film. Despite this slight increase, the MoS_2/Ag/WC film achieves the lowest wear rate (2.0×10^{-7} mm^3 N^{-1} m^{-1}), surpassing the performance of state-of-the-art MoS_2-based materials under the similar test conditions.[49–53] As depicted in Fig. 8(D) and Fig. S13C (ESI†), the wear profile and morphology of MoS_2/WC film show many deep grooves, indicative of typical abrasive wear characteristics. In contrast, the wear track of the MoS_2/Ag/WC film appears relatively shallow and smooth (Fig. 8(D) and Fig. S13D in the ESI†), suggesting that Ag contributes to repairing the sliding interface and reducing the probability of abrasive wear.[54,55] However, as the Ag content increased, larger Ag particles form, which disrupts the formation of a stable sliding interface and leads to obvious fluctuations in the friction coefficient (Fig. S14 in the ESI†).

After 21 days of salt spraying, the MoS_2/WC film shows a high friction coefficient during the running-in stage (Fig. 8(A)) due to the formation of numerous surface corrosion pits (Fig. 4(D)), which hinders the development of a continuous tribofilm on the counterpart steel ball (inset in Fig. 8(E)). By comparison, the friction coefficient of the MoS_2/Ag/WC film stabilizes quickly after a short running-in period (Fig. 8(A)). This behavior can be attributed to its superior corrosion resistance during prolonged salt exposure. The diffusion and repairing action of Ag result in a denser and smoother film surface (Fig. 4(E)), facilitating the rapid establishment of a stable tribofilm at the sliding interface. During the stable stage, the friction coefficients of both nano-multilayer films are

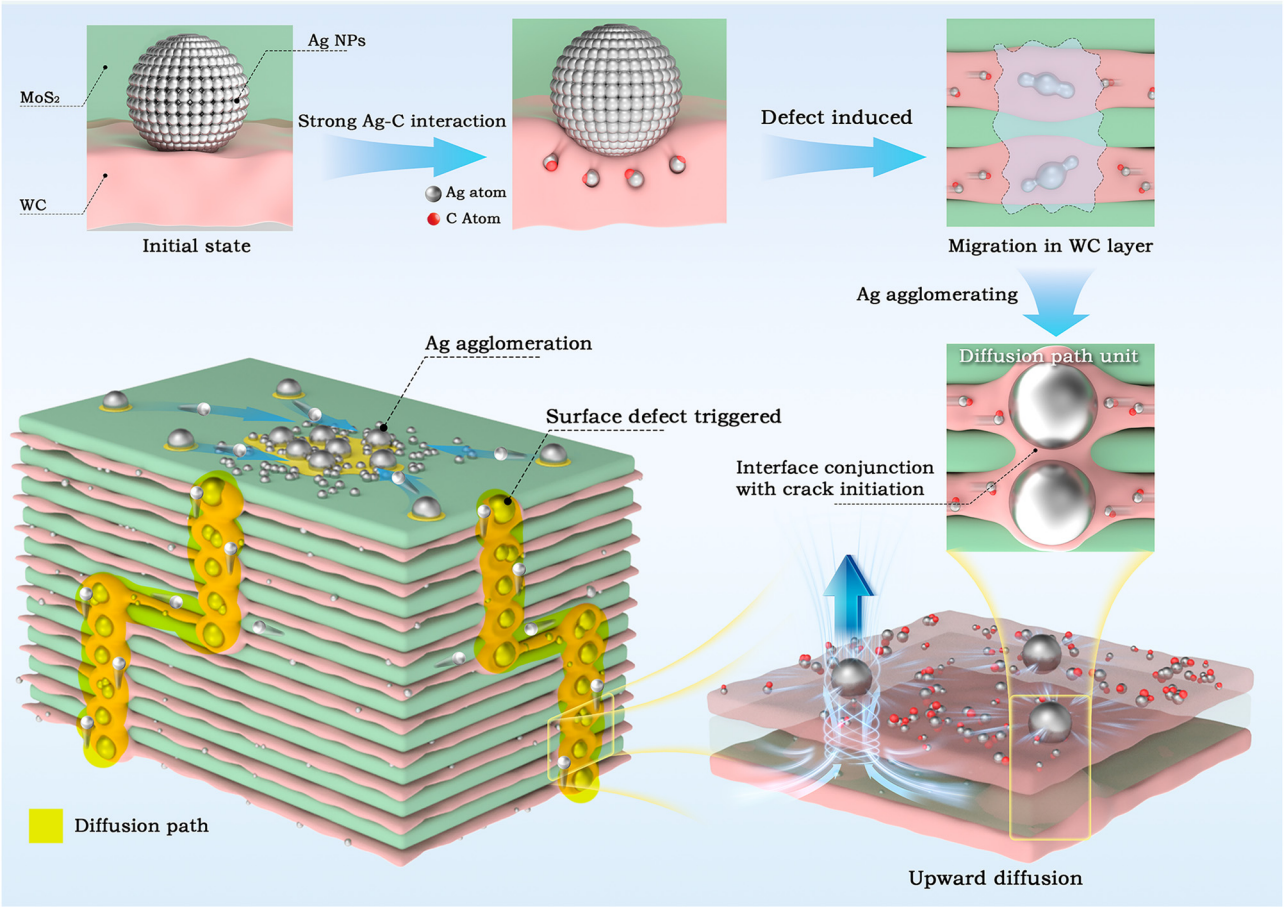

Fig. 7 Schematic of defect-dominated diffusion kinetics of Ag atoms within the sandwich-like MoS_2/Ag/WC nanomultilayer film.

comparable to those observed before salt spraying (Fig. 8(A) and (B)). However, the wear rate of the MoS_2/WC film increases by 2.3 times after salt spraying (Fig. 8(B)), with instances of exfoliation observed in localized areas (Fig. 8(E) and Fig. S15 in the ESI†). This effect is closely linked to the numerous corrosion pits formed on the film (Fig. 4(D)). The generated wear debris embedded into these pits during frictional processes leads to local film exfoliation under periodic high contact stress. In comparison, MoS_2-based films fabricated by references exhibit significant corrosion, discoloration, and peeling from the steel substrate after only 14 days of salt spray exposure.[49–53] The tribological properties deteriorate markedly, with some films failing prematurely (Fig. 8(C) and Fig. S16, S17 in the ESI†). In stark contrast, sandwich-like MoS_2/Ag/WC nanomultilayer film shows a flat and smooth wear track after 21 days of salt spray, accompanied by the formation of a continuous and compact tribofilm on the counterpart ball surface (Fig. 8(F)). These characteristics enhance its superior frictional and wear-resistant properties.

In the context of salt spraying and friction tests, Raman spectra were acquired at specific positions along the film wear tracks and ball wear scars. Analysis reveals two prominent peaks near 375 cm^{-1} and 415 cm^{-1} (Fig. 8(F)), attributed to the E^1_{2g} and A_{1g} modes of MoS_2, respectively.[56,57] Another peak appeared at ~531 cm^{-1} is associated with the second-order (E_{1g} + LA(M)) mode of MoS_2.[58] Notably, the wear scars of both films show strong signals of metal oxides (MeO_x, *e.g.*, WO_3 or MoO_3).[23] These findings suggest that the defective MoS_{2-x} and WC_{1-x} within the film undergo oxidation in the presence of oxygen and water under high contact pressure, resulting in the formation of MeO_x. Therefore, the sliding interface is dominated by MoS_2 nanosheets and MeO_x nanoparticles, consistent with previous reports,[23,59] contributing significantly to achieving low friction.

2.6 Friction and wear mechanisms of the sandwich-like nanomultilayer film

To verify the mechanisms underlying the observed low friction coefficient and minimal wear damage after salt spraying, the formed tribofilm adhering to the counterpart ball surface was further characterized by TEM. The overall cross-sectional micrograph in Fig. 9(A) provides a clear depiction of the lamellar structure, including a ball substrate, a ~750 nm thick tribofilm, and a carbon protective layer. EDS mapping analysis (Fig. 9(B)) confirms even distribution of Mo, W, Ag, and S elements throughout the tribofilm. Notably, oxygen enrichment across the tribofilm indicates oxide formation, consistent with the Raman spectra results (Fig. 8(F)). Fig. 9(C) illustrates the

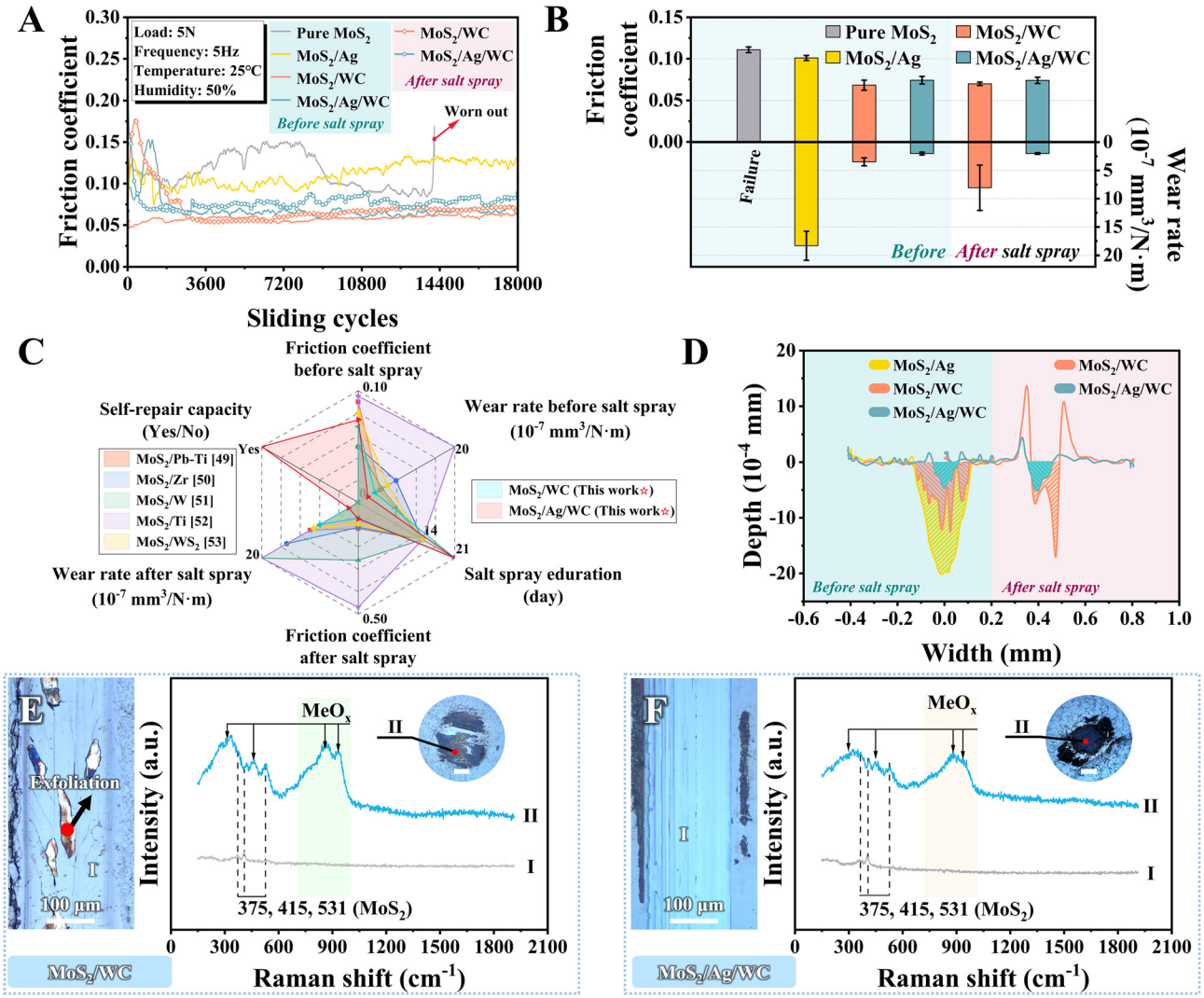

Fig. 8 Tribological properties of sandwich-like MoS_2/Ag/WC nanomultilayer film and reference films before and after salt spray tests. (A) and (B) Friction curves, average friction coefficients and wear rates before and after salt spray tests. (C) Comparison analysis of tribological performance of the sandwich-like MoS_2/Ag/WC nano-multilayer film *versus* previously reported MoS_2-based films, both before and after salt spray testing.[49–53] (D) 2D profiles demonstrating the cross-sectional view of film wear tracks before and after salt spray tests, with slashes signifying the corresponding wear volume. (D) and (E) Optical images showing film wear tracks (I) and ball wear scars (II) of MoS_2/WC and MoS_2/Ag/WC nanomultilayer films after salt spray tests, with corresponding Raman spectra identified in marked positions. All the scale bars are of 100 μm.

uniform compactness of the ~750 nm thick tribofilm, revealing no discernible pores or gaps. This uniformity suggests that the presence of Ag facilitates the transfer and adhesion of the film during the sliding process. Moreover, the enhanced mobility of Ag under frictional heat and high contact stress helps to repair pores and defects within the tribofilm,[60] as evidenced in Fig. 9(B), which demonstrates the uniform distribution of Ag elements.

HRTEM imaging of the marked blue square reveals abundant stripes identified as MoS_2 nanosheets and dark spots as MeO_x nanoparticles (Fig. 9(D)), distinguished by their atomic spacing. Many MeO_x nanoparticles are positioned at the contact interface, sliding with MoS_2 (002) nanosheets to form numerous incommensurate MoS_2/MeO_x nanocontacts,[23] crucial for achieving low friction in humid air. Fig. 9(E) illustrates larger MeO_x nanoparticles, initially observed as black spots in Fig. 9(C), within the tribofilm. These larger nanoparticles exhibit a core–shell structure enveloped by MoS_2 nanosheets under frictional conditions, effectively preventing abrasive wear and reducing wear rates. EDS line scanning across the marked white rectangle in Fig. 9(E) shows a heightened Ag signal around the periphery of the nanoparticles (Fig. 9(F)). This indicates that Ag not only fills pores and defects in the tribofilm, enhancing its density, but also serves as a stitching agent facilitating adhesion between MoS_2 nanosheets and the MeO_x. Such MoS_2/MeO_x dominated contact interface further mitigates abrasive wear, resulting in low friction and minimal wear.

Based on the superior corrosion resistance and self-repairing properties of the sandwich-like film, we conducted a long-term (200 000 cycles) friction test on MoS_2/WC and

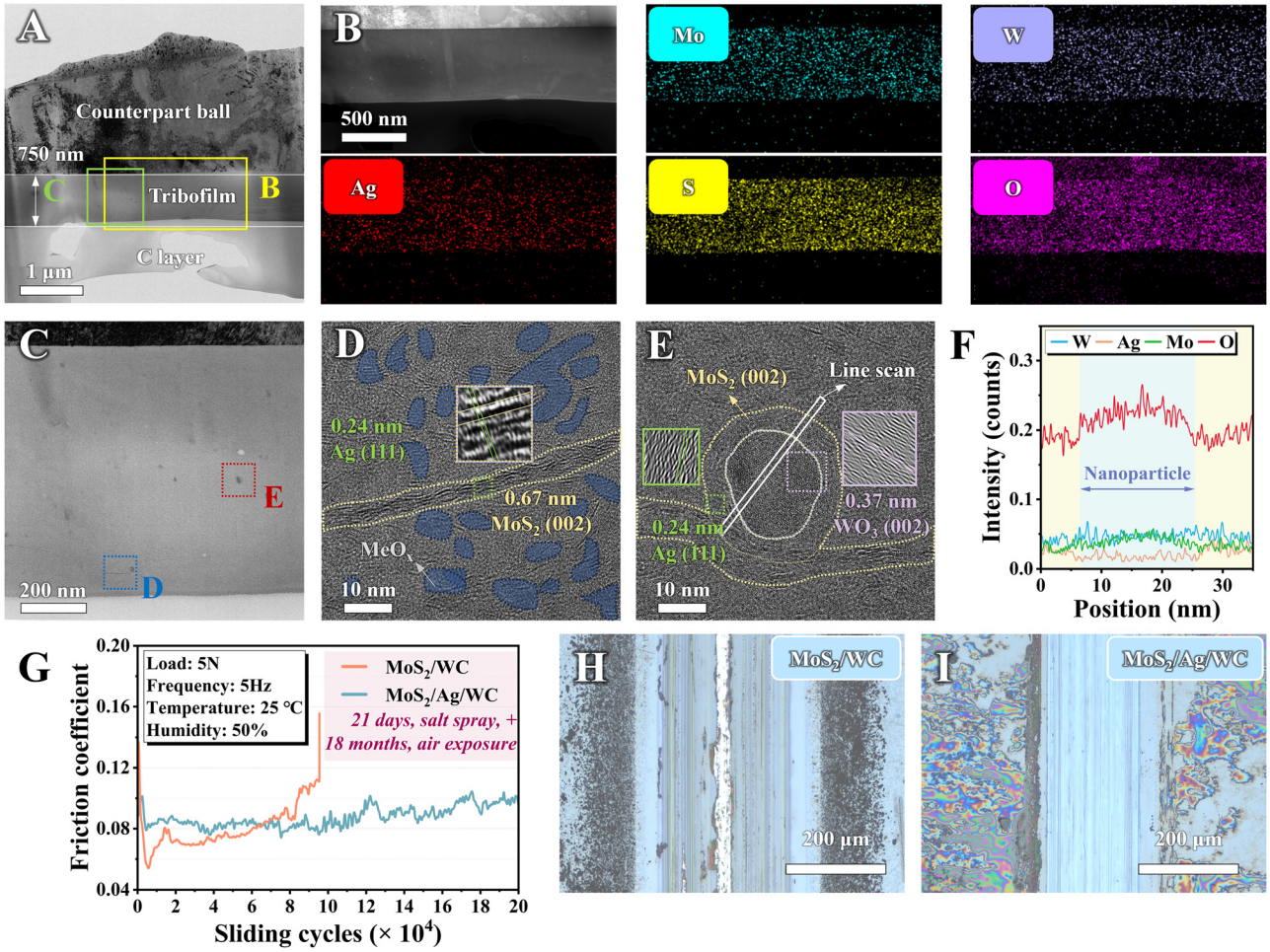

Fig. 9 Mechanisms of low friction and wear of the sandwich-like MoS_2/Ag/WC nanomultilayer film. (A) Low magnification TEM image showing overall cross-sectional view of the tribofilm formed after the salt spray test. (B) STEM-HAADF image of the region marked by the yellow rectangle in (A), accompanied by elemental maps highlighting Mo, W, Ag, S, and O distributions. (C) Enlarged view of the region marked by the green square in (A), illustrating the dense structure dispersed with particles. (D) and (E) HRTEM images identified on the labelled dashed squares in (C). (F) EDS line scanning plot of the marked white rectangle in (E). (G) Friction curves obtained from a long-term tribological test (200 000 cycles) of MoS_2/WC and MoS_2/Ag/WC nanomultilayer films following a 21-day salt spray test and 18 months of air exposure. (H) and (I) Optical images of film wear tracks of MoS_2/WC and MoS_2/Ag/WC nanomultilayer films after the long-term tribological test, respectively.

MoS_2/Ag/WC nanomultilayer films following a 21-day salt spray test and 18 months of air exposure. Fig. 9(G) shows that the MoS_2/WC film fails to complete the sliding mission in a humid environment, ceasing at ~97 000 cycles, as evidenced by the optical image in Fig. 9(H). In contrast, the MoS_2/Ag/WC film maintains a relatively stable friction coefficient throughout the entire test period. After 200 000 sliding cycles, the wear track exhibits shallow grooves due to the action of formed MeO_x under high contact pressure during a prolonged frictional process. The corresponding wear rate of the sandwich-like film reaches an ultra-low level of 1.25×10^{-7} mm^3 N^{-1} m^{-1} (Fig. S18, ESI†). This demonstration shows that the sandwich-like film can repair surface defects through the spontaneous diffusion of Ag, exhibiting superior corrosion resistance compared to other state-of-the-art MoS_2-based materials. This characteristic enables the film to sustain the lubricating performance of MoS_2, whether subjected to salt spraying or extended air exposure.

3. Conclusions

In summary, we have successfully designed and prepared a MoS_2/Ag/WC nanomultilayer film with a sandwich-like structure. This novel architecture exhibits superior resistance to microplastic deformation, extraordinary environmental adaptability, and robust tribological performance. The spontaneous diffusion of Ag atoms within the amorphous WC layer and defects of the film, along with the self-repairing capability of Ag, ensure that the film remains virtually free from oxidation after exposure to a salt spray corrosion environment for 21 days and atmospheric conditions for 18 months, outperforming its competitor. Importantly, the film maintains a low friction coefficient and an ultra-low wear rate (1.25×10^{-7} mm^3 N^{-1} m^{-1}) even after harsh corrosion tests. This performance is attributed to the adhesion of the Ag-assisted film material on the counterpart ball, the repair of pores and defects in the tribofilm, resulting in a uniform and dense tribofilm. Additionally, friction induces the

formation of a sliding interface comprised of highly oriented MoS_2 nanosheets in contact with or wrapping MeO_x nanoparticles, creating numerous incommensurate nanocontacts. This contact interface not only prevents abrasive wear but also achieves sustained low friction and wear properties. Our findings pave the way for the long-term applications of solid lubricating films in corrosive environments, offering significant engineering relevance.

4. Experimental details

Sample preparation

Sandwich-like MoS_2/Ag/WC nanomultilayer films were fabricated using a Teer CF-800 unbalanced magnetron sputtering system (Droitwich, UK). The deposition sequence involved targets of one Ag (99.99% purity, Zhongnuo Advanced Material Technology Co., Ltd, China), one WC (99.99% purity, China Material Technology Co., Ltd), one MoS_2 (99.99% purity, China Material Technology Co., Ltd), one Ti (99.99% purity, China Material Technology Co., Ltd), and two MoS_2 (99.99% purity, China Material Technology Co., Ltd), as illustrated in Fig. 1. Prior to deposition, substrates were prepared by ultrasonic cleaning in acetone and alcohol for 20 min each, followed by argon plasma etching with a substrate pulsed bias of −500 V for 30 min to remove surface contaminations. The substrate temperature was maintained at 150–200 °C. The resultant film successively consisted of a Ti interlayer (Ti target current set at 5 A, deposited for 15 min), a Ti/MoS_2/Ag/WC gradient transition layer (target currents: Ti: 5 A to 0 A, MoS_2: 0 A to 1.6 A, Ag: 0 A to 0.2 A, WC: 0 A to 0.8 A, deposited for 30 min), and a sandwich-like MoS_2/Ag/WC nanomultilayer (target currents: MoS_2: 1.6 A, Ag: 0.2 A, WC: 0.8 A, deposited for 100 min). Sample holder rotation speeds were maintained at 5 rpm, 2 rpm, and 0.5 rpm for each respective deposition stage. The resulting structure comprised 49 MoS_2/WC bilayers with Ag NPs randomly dispersed between the layers. Reference samples, including MoS_2, MoS_2/WC, and MoS_2/Ag films, were prepared under identical deposition conditions for comparative analysis.

Characterization

Cross-sectional and surface morphologies, accompanied by composition analysis of films, were investigated using a field emission SEM (FESEM, FEI Quanta FEG 250) equipped with EDS. For comprehensive structural and elemental analysis, TEM (Talos F200x, 200 kV) and spherical aberration-corrected (AC-TEM, Spectra 300, 200 kV) equipped with HAADF detectors and EDS were employed. TEM samples were prepared *via* a FIB milling (Helios-G4-CX). Atomic resolution 3D reconstruction and elemental analysis were carried out using APT. The APT specimens were prepared by Ga FIB milling, with a controlled removal of the superficial part to ensure stable testing. APT measurements were performed under UV laser pulsing (355 nm), with a pulse energy of 200 pJ, a pulse repetition rate of 200 kHz, and a target evaporation rate of 0.1% per pulse at 50 K. The reconstruction and quantitative analysis of APT data were carried out using a CAMECA visualization and analysis software (AP Suite 6.3.2.125).

Surface topographies, surface potentials, and corresponding 2D/3D images were acquired using an SPM (Bruker Dimension ICON). Analysis of roughness and potential variations was conducted *via* a Bruker data processing software (Nanoscope Analysis version 2.00). Structural properties, chemical bonding, and composition analysis of the films were investigated using XRD with Cu Kα radiation (D8 DISCOVER, 5–70°), micro-Raman spectroscopy (Renishaw inVia Reflex, wavelength 532 nm), and XPS (AXIS ULTRA DLD). The surface morphologies of film wear tracks and ball wear scars were determined utilizing a laser scanning confocal microscope (Zeiss, LSM 700).

Salt spray tests

Salt spray tests were conducted in a Q-LAB CCT1100 corrosion cycling test chamber following ASTM B117 standard to evaluate the environmental stability of as-deposited films. Prior to testing, areas not covered by the film were sealed with waterproof tapes to prevent salt spray permeation. The salt spray was generated using a 5 wt% NaCl solution and introduced into the test chamber maintained at a constant temperature of 35 ± 2 °C, resulting in chamber pressures ranging from 69 to 172 kPa and humidity levels between 80 and 90%. Each film was assessed with three reference samples, all positioned at a 75° angle to the horizontal axis within the chamber for 21 days.

Mechanical tests

Indentations on the films were performed using a nanoindenter (MTS G200) equipped with a Berkovich diamond tip. Six individual indentations were conducted for each sample with a consistent indentation force of 50 mN. Nano wear tests were conducted employing a multi-pass method, stepwisely increasing the normal load during testing *via* SPM (Dimension ICON), as reported previously.[40] The testing utilized conical diamond nano-indenting tips (Bruker, DNISP-HS) with a nominal radius of ~40 nm. The normal force F_N was generated by converting voltage signals following the formula:[61]

$$F_N = K_N S V_N,$$

where the K_N (calibrated as 68.24 N m^{-1}) represents the normal spring constant of the probe, S denotes the sensitivity calculated as 208.4 nm V^{-1}, and V_N signifies the normal voltage of photodiode.[62]

The normal load was increased from 500 nN to 15 μN across 16 equal passes within a 2 × 2 μm^2 square area, with corresponding loading images captured in real-time. Topographical differences of the testing region were further scanned by tapping mode using the monocrystalline silicon probe (Bruker, RTESPA-300, 8 nm radius, 40 N m^{-1}) before and after nano friction tests. Each data point presented in Fig. 3(E) and (F) represents the average results obtained from three independent experiments, ensuring statistical reliability.

Tribological tests

Reciprocating friction tests of the MoS_2/Ag/WC film and its reference samples were carried out using a CSM tribometer under ambient conditions (25 ± 3 °C, ~50% RH). The tests

were performed against GCr15 steel balls (Φ6 mm) with an amplitude of 5 mm, an applied load of 5 N, and a frequency of 5 Hz, respectively. The corresponding wear rates (W) were calculated from the cross-sectional area of the wear tracks (AlphaStep IQ surface profiler) following the formula:

$$W = \Delta V/(F \times S),$$

where W signifies the wear rate ($mm^3\ N^{-1}\ m^{-1}$), ΔV denotes the worn volume of the film (mm^3), F represents the applied normal load (N), and S is the full sliding distance (m).

Vacuum annealing acceleration tests

Vacuum annealing tests were performed *via* a tube furnace (BTF-1200 C, BEQ Company, China) to evaluate the diffusion behavior of Ag within MoS_2/Ag/WC nanomultilayer film. For each test, samples were heated at a controlled rate of 2 °C per minute to temperatures of 200 °C and 300 °C, respectively. These temperatures were maintained for 30 minutes under a background vacuum of less than 1×10^{-3} Pa before cooling to room temperature.

Author contributions

Min Yang: data curation, validation, formal analysis, investigation, methodology, and writing – original draft. Xin Fan: formal analysis and writing – original draft. Siming Ren: conceptualization, resources, formal analysis, funding acquisition, investigation, methodology, supervision, and writing – review & editing. Liping Wang: conceptualization, funding acquisition, supervision, and writing – review & editing.

Data availability

The data supporting this article have been included as part of the ESI.†

Conflicts of interest

There are no conflicts to declare.

Acknowledgements

This work was financially supported by the National Science Fund for Distinguished Young Scholars of China (No. 52425501), the National Natural Science Foundation of China (No. 52375220, U21A20127), and the Strategic Priority Research Program of the Chinese Academy of Sciences (No. XDB 047030202).

References

1 M. R. Cai, Q. L. Yu, W. M. Liu and F. Zhou, *Chem. Soc. Rev.*, 2020, **49**, 7753–7818.
2 J. B. Luo, M. Liu and L. R. Ma, *Nano Energy*, 2021, **86**, 106092.
3 S. W. Chen, H. Sun, J. Liu, J. Y. Wang, H. S. Lu, J. C. Hao, L. Xu and W. M. Liu, *Mater. Horiz.*, 2024, **11**, 1668–1678.
4 W. Z. Zhai and K. Zhou, *Adv. Funct. Mater.*, 2019, **29**, 1806395.
5 D. Duncan, *History of Tribology*, Professional Engineering Publishing, London, 1998.
6 M. R. Vazirisereshk, A. Martini, D. A. Strubbe and M. Z. Baykara, *Lubricants*, 2019, **7**, 57.
7 J. M. Martin, C. Donnet, T. Lemogne and T. Epicier, *Phys. Rev. B: Condens. Matter Mater. Phys.*, 1993, **48**, 10583–10586.
8 H. Li, J. H. Wang, S. Gao, Q. Chen, L. M. Peng, K. H. Liu and X. L. Wei, *Adv. Mater.*, 2017, **29**, 1701474.
9 C. Lee, Q. Y. Li, W. Kalb, X. Z. Liu, H. Berger, R. W. Carpick and J. Hone, *Science*, 2010, **328**, 76–80.
10 Z. X. Yang, X. K. Zhang, K. X. Gao, B. Zhang, F. G. Sen, S. Bhowmick, J. Y. Zhang and A. T. Alpas, *ACS Appl. Mater. Interfaces*, 2024, **16**, 13267–13281.
11 X. L. Zhang, T. H. Ren and Z. P. Li, *J. Mater. Chem. A*, 2023, **11**, 9239–9269.
12 S. Ren, Z. Gao, X. Fan, H. Wang and L. Wang, *Sci. China: Technol. Sci.*, 2024, **67**, 2018–2030.
13 N. X. Wei, H. Li, J. L. Li, L. L. Sun, J. W. Huang, J. Kong, Q. J. Wu, Y. Shi and D. S. Xiong, *Appl. Surf. Sci.*, 2024, **646**, 158905.
14 S. M. Ren, W. T. Cao, M. J. Cui and H. X. Wang, *Surf. Coat. Technol.*, 2023, **458**, 129317.
15 J. Shi, R. Q. Zhao, Z. X. Yang, J. Z. Yang, W. H. Zhang, C. B. Wang and J. Y. Zhang, *Mater. Horiz.*, 2023, **10**, 4148–4162.
16 S. M. Ren, H. Li, M. J. Cui, L. P. Wang and J. B. Pu, *Appl. Surf. Sci.*, 2017, **401**, 362–372.
17 P. Series, E. Nicholson, J. Tarn, N. Barri, J. B. Chemin, G. R. Wang, Y. Michel, C. V. Singh, P. Choquet, A. Saulot, T. Filleter and G. Colas, *Adv. Funct. Mater.*, 2022, **32**, 2110429.
18 J. F. Curry, M. A. Wilson, H. S. Luftman, N. C. Strandwitz, N. Argibay, M. Chandross, M. A. Sidebottom and B. A. Krick, *ACS Appl. Mater. Interfaces*, 2017, **9**, 28019–28026.
19 E. Serpini, A. Rota, S. Valeri, E. Ukraintsev, B. Rezek, T. Polcar and P. Nicolini, *Tribol. Int.*, 2019, **136**, 67–74.
20 M. Khadem, O. V. Penkov, J. Jais, S. M. Bae, V. S. Dhandapani, B. Kang and D. E. Kim, *Sci. Adv.*, 2021, **7**, eabk1224.
21 Z. C. Gao, J. Buchinger, N. Koutná, T. Wojcik, R. Hahn and P. H. Mayrhofer, *Acta Mater.*, 2022, **231**, 117871.
22 Z. R. Gao, W. M. Nie, H. X. Wang, S. M. Ren, D. L. Du, S. Y. Du and J. L. Li, *Composites, Part B*, 2024, **275**, 111350.
23 S. M. Ren, M. J. Cui, A. Martini, Y. B. Shi, H. X. Wang, J. B. Pu, Q. Y. Li, Q. J. Xue and L. P. Wang, *Cell Rep. Phys. Sci.*, 2023, **4**, 101390.
24 D. X. Zhu, J. Zhang, P. P. Li, Z. Li, H. X. Li, X. H. Liu, T. B. Ma, L. Ji, H. D. Zhou and J. M. Chen, *Adv. Funct. Mater.*, 2024, **34**, 2316036.
25 S. M. Ren, M. J. Cui, C. B. Liu and L. P. Wang, *Corros. Sci.*, 2023, **212**, 110939.
26 S. Utrera-Barrios, R. Verdejo, M. A. López-Manchado and M. H. Santana, *Mater. Horiz.*, 2020, **7**, 2882–2902.

27 F. J. Li, X. H. Yu, X. W. Shi, D. Sun, H. J. Du, Y. Shao, J. B. Wang and S. M. Zhang, *Surf. Coat. Technol.*, 2023, **466**, 129654.
28 Z. C. Hu, J. W. Fu, L. Cheng, D. G. Ding, J. K. Cong, D. R. Yang and X. G. Yu, *Phys. Status Solidi A*, 2024, **221**, 2300738.
29 J. Ma and S. H. Wei, *Phys. Rev. Lett.*, 2013, **110**, 235901.
30 K. Sbiaai, Y. Boughaleb, M. Mazroui, A. Hajjaji and A. Kara, *Thin Solid Films*, 2013, **548**, 331–335.
31 T. W. Wang and P. D. Bristowe, *Acta Mater.*, 2017, **137**, 115–122.
32 C. T. Chen, S. Nagao, K. Suganuma, J. T. Jiu, H. Zhang, T. Sugahara, T. Iwashige, K. Sugiura and K. Tsuruta, *Appl. Phys. Lett.*, 2016, **109**, 093503.
33 S. A. Odom, S. Chayanupatkul, B. J. Blaiszik, O. Zhao, A. C. Jackson, P. V. Braun, N. R. Sottos, S. R. White and J. S. Moore, *Adv. Mater.*, 2012, **24**, 2578–2581.
34 Y. B. Zhu, M. P. Dong, X. R. Zhao, J. L. Li, K. K. Chang and L. P. Wang, *J. Am. Ceram. Soc.*, 2019, **102**, 7521–7532.
35 H. J. Gong, C. C. Yu, L. Zhang, G. X. Xie, D. Guo and J. B. Luo, *Composites, Part B*, 2020, **202**, 108450.
36 T. Zhu, K. Wu, Y. Q. Wang, J. Y. Zhang, G. Liu and J. Sun, *Mater. Horiz.*, 2023, **10**, 5920–5930.
37 S. S. Xu, L. Q. Yang, Y. Z. Liu, Y. Hua, X. M. Gao and A. Neville, *J. Mater. Chem. A*, 2020, **8**, 19473–19483.
38 M. A. Baker, R. Gilmore, C. Lenardi and W. Gissler, *Appl. Surf. Sci.*, 1999, **150**, 255–262.
39 S. Domínguez-Meister, T. C. Rojas, J. E. Frías and J. C. Sánchez-López, *Tribol. Int.*, 2019, **140**, 105837.
40 Q. Jia, W. H. He, D. P. Hua, Q. Zhou, Y. Du, Y. Ren, Z. B. Lu, H. F. Wang, F. Zhou and J. Wang, *Acta Mater.*, 2022, **232**, 117934.
41 R. Z. Valiev, R. K. Islamgaliev and I. V. Alexandrov, *Prog. Mater. Sci.*, 2000, **45**, 103–189.
42 P. P. Weng, X. C. Yin, W. Hu, H. Yuan, C. Q. Chen, H. P. Ding, B. Yu, W. H. Xie, L. Jiang and H. Wang, *Tribol. Int.*, 2021, **162**, 107114.
43 B. Wu, A. Heidelberg and J. J. Boland, *Nat. Mater.*, 2005, **4**, 525–529.
44 J. Zhang, Z. F. Li, C. B. Zhang, L. D. Shao and W. R. Zhu, *npj 2D Mater. Appl.*, 2022, **6**, 47.
45 M. Z. Zhao, Z. B. Zhang, W. J. Shi, Y. W. Li, C. W. Xue, Y. X. Hu, M. C. Ding, Z. Q. Zhang, Z. Liu, Y. Fu, C. Liu, M. H. Wu, Z. K. Liu, X. Z. Li, Z. J. Wang and K. H. Liu, *Nat. Commun.*, 2023, **14**, 7447.
46 M. J. Hwang, E. J. Park, W. J. Moon, H. J. Song and Y. J. Park, *Corros. Sci.*, 2015, **96**, 152–159.
47 X. C. Chen, X. Yin, W. Qi, C. H. Zhang, J. Choi, S. D. Wu, R. Wang and J. B. Luo, *Sci. Adv.*, 2020, **6**, eaay1272.
48 Y. X. Wu, Y. Liu, H. X. Li, J. M. Chen, S. W. Yu, B. Zhou and B. Tang, *Tribol. Int.*, 2016, **101**, 395–401.
49 K. D. Shang, S. X. Zheng, S. M. Ren, J. B. Pu, D. Q. He and S. Liu, *Appl. Surf. Sci.*, 2018, **437**, 233–244.
50 L. Li, Z. X. Lu, J. B. Pu and B. R. Hou, *Appl. Surf. Sci.*, 2021, **541**, 148453.
51 C. Zeng, J. B. Pu, H. X. Wang, S. J. Zheng, L. P. Wang and Q. J. Xue, *Ceram. Int.*, 2019, **45**, 15834–15842.
52 H. Li, G. G. Zhang and L. P. Wang, *J. Phys. D: Appl. Phys.*, 2016, **49**, 095501.
53 C. Zeng, J. B. Pu, H. X. Wang, S. J. Zheng and R. Chen, *Ceram. Int.*, 2020, **46**, 13774–13783.
54 M. H. Zhou, R. T. Tong, T. Zhang and G. Liu, *Front. Mech. Eng.*, 2023, **18**, 39.
55 N. Xiao, C. H. Zhang, X. Yin, K. Yang, F. Z. Zhang and B. Y. Xiong, *Mater. Sci. Eng., B*, 2023, **295**, 116600.
56 H. Li, Q. Zhang, C. C. R. Yap, B. K. Tay, T. H. T. Edwin, A. Olivier and D. Baillargeat, *Adv. Funct. Mater.*, 2012, **22**, 1385–1390.
57 M. Dieterle, G. Weinberg and G. Mestl, *Phys. Chem. Chem. Phys.*, 2002, **4**, 812–821.
58 X. Fan, Y. B. Shi, M. J. Cui, S. M. Ren, H. X. Wang and J. B. Pu, *ACS Appl. Nano Mater.*, 2021, **4**, 10307–10320.
59 Z. R. Gao, W. M. Nie, H. X. Wang, S. M. Ren, D. L. Du, S. Y. Du and J. L. Li, *Composites, Part B*, 2024, **275**, 111350.
60 X. Yang, H. L. Liu, L. M. Zhang, Y. R. Hu, D. J. Politis, M. M. Gharbi and L. L. Wang, *Friction*, 2024, **12**, 375–395.
61 H. E. Ko, H. W. Park, J. Z. Jiang and A. Caron, *Acta Mater.*, 2018, **147**, 203–212.
62 H. E. Ko, S. G. Kwan, H. W. Park and A. Caron, *Friction*, 2018, **6**, 84–97.